Chapter 4

Simulation and Experimental Results

4.1 Introduction

As mentioned earlier in Chapter 1, attempts at possible on-chip filters have particularly been demonstrated for 10.7 MHz IF filters. Chapter 2 have examined current technologies and research efforts. Chapter 3 have presented a new realization of a high-Q bandpass filter and new circuit realizations for fully balanced high-Q wide-dynamic-range current-tunable Gm-C bandpass filters through Techniques 1 and 2 as shown in Figures 3.2 and 3.3, respectively.

In this chapter, simulation and experimental results of Techniques 1 and 2 are presented for 10.7-MHz fully balanced high-Q wide-dynamic-range current-tunable Gm-C bandpass filters. Section 4.2 describes experimental preparations for measured performances of Techniques 1 and 2. Simulation and experimental results of Techniques 1 and 2 in terms of measured quality factors, current-tunable center frequencies, noise performance and dynamic ranges are described in Sections 4.3, 4.4, 4.5 and 4.6, respectively. Section 4.7 presents the temperature compensation for the center frequencies and the quality factors of Techniques 1 and 2. Preliminary interpolation of power consumption and dynamic ranges are predicted in Section 4.8. Section 4.9 describes high frequency simulation of Techniques 1 and 2. Section 4.10 shows physical layouts of the circuits in Technique 1 and 2 and shows the corresponding simulations. Comparisons to other 10.7-MHz Gm-C approaches are presented in Section 4.11.

4.2 Experimental Preparations

The center frequency f_o, the bandwidth BW at f_o and the output noise power of Techniques 1 and 2 are measured using a spectrum analyzer and a tacking generator. A set-up for the measurement of the third-order intermodulation IM_3 of the filter is shown in Figure 4.1 using two sinusoidal generators (f_1 and f_2), a standard power combiner and a spectrum analyzer. The two signals (f_1 and f_2) are combined by the power combiner and fed into the filter under test. Then, the third-order intermodulation product at $|2f_1 - f_2|$ is observed on the spectrum analyzer.

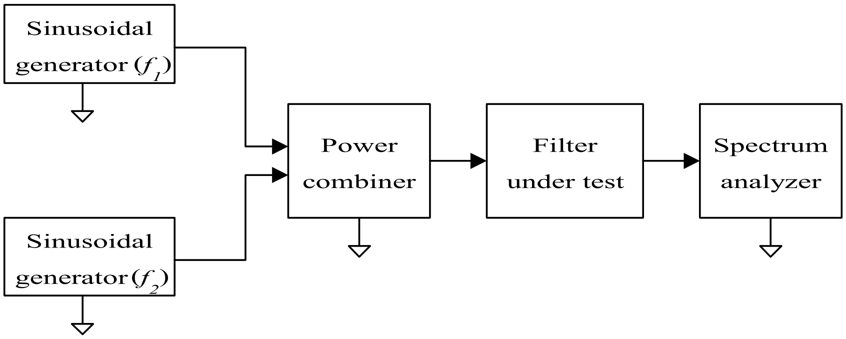

Figure 4.1 A setup for the measurement of the filter under test

Figure 4.2 shows a circuit implementation of Technique 1 shown in Figure 3.2. Figure 4.3 shows a circuit implementation of Technique 2 shown in Figure 3.3. All transistors are modeled by a simple low noise transistor 2N2222 where the average transition frequency (f_T) is 120 MHz and β is approximately 120 (Small-Signal Transistor Data, Philips Inc., 2001). All current sinks are LM334 (National Semiconductor Data, 2000). The supply voltage V_{CC}= 6 V, V_{EE} = -6 V, the bias current I_1 = 1 mA, I_2 = 1 mA and C_1 = 150 pF.

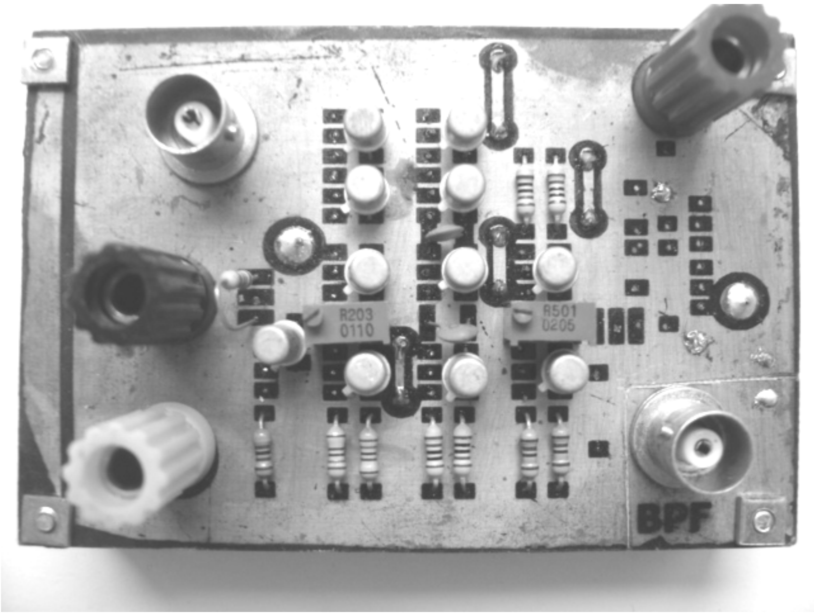

Figure 4.2 A circuit implementation of Technique 1 shown in Figure 3.2.

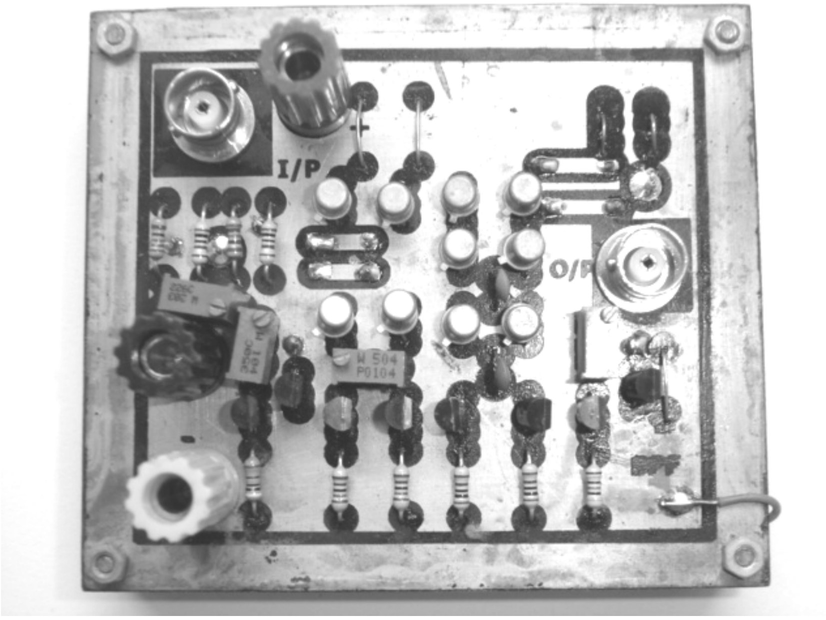

Figure 4.3 A circuit implementation of Technique 2 shown in Figure 3.3.

4.3 Measured Quality Factors

4.3.1 High Quality Factor Q_{HQ1} of Technique 1

Figure 4.4 illustrates the measured frequency response of Technique 1 of a fully balanced high-Q current-tunable Gm-C bandpass filter shown in Figure 3.2 at the center frequencies $f_0 = \omega_{HQ}/(2\pi) = 10.7$ MHz and the power consumption P_{C1}=60 mW. It can be seen from Figure 4.2 that the bandwidth (BW1) are 2×44 = 88 kHz and therefore the measured quality factor Q_{HQ1} ($=f_0/BW1$) is relatively high at approximately 121 which is consistent with the value of β =120.

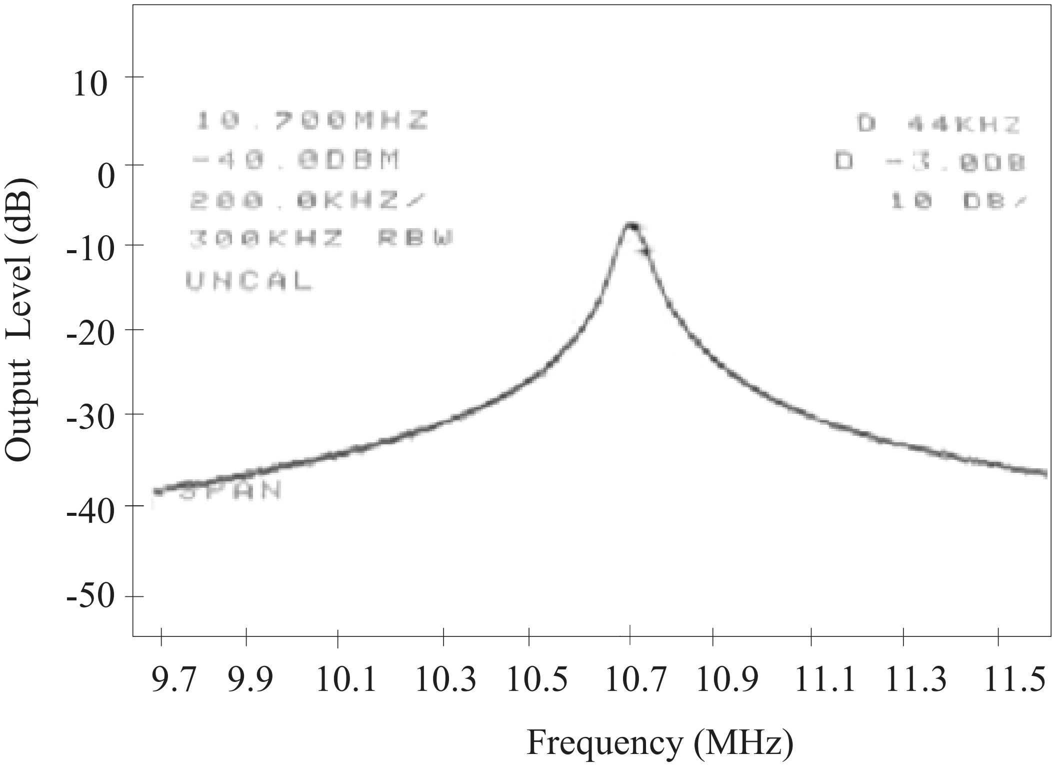

Figure 4.4 A measured frequency response at the center frequency f_0=10.7 MHz and the quality factor Q_{HQ1} = 121 of Technique 1 shown in Figure 3.2.

Figure 4.5 plots the quality factor Q_{HQ1} of the analysis and the PSPICE simulated results of Technique 1 shown in Figure 3.2 versus the common-emitter current gain. The common-emitter current gain may be separated into β_{max} and $\beta(\omega)$ where $\beta(\omega) = \beta_{max}/(1+j\omega[C_{j\_BE} + C_{d\_BE}]r_{\pi})$, β_{max} is the maximum common-emitter current gain, C_{j_BE} is the junction capacitance, C_{d_BE} is the diffusion capacitance and r_{π} is the input impedacne of a transistor. It can be seen from Figure 4.5 that a maximum common-emitter current gain β_{max} of 190, the upper limit of the quality factor Q_{HQ1} can be expected at approximately 160.

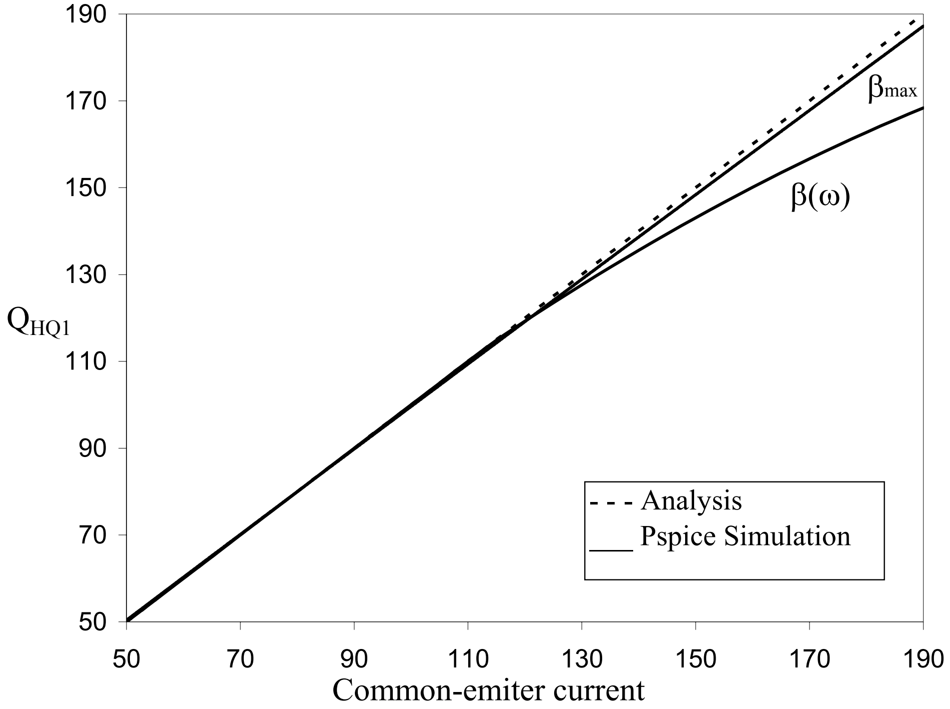

Figure 4.5 Plots of the quality factor Q_{HQ1} versus the common-emitter current gain of Technique 1 shown in Figure 3.2.

4.3.2 High Quality Factor Q_{HQ2} of Technique 2

Figure 4.6 illustrates the measured frequency response of Technique 2 of a fully balanced high-Q current-tunable Gm-C bandpass filter shown in Figure 3.3 where $R_C = 50\ \Omega$, the bias current $2I_3$ = 1 mA and the power consumption P_{C2}=70 mW at the center frequencies $f_0 = \omega_{HQ}/(2\pi)$ = 10.7 MHz. It can be seen from Figure 4.6 that the bandwidth (BW2) are 2×24 = 48 kHz and therefore the measured quality factor Q_{HQ2} (=f_0/BW2) is relatively high at approximately 223.

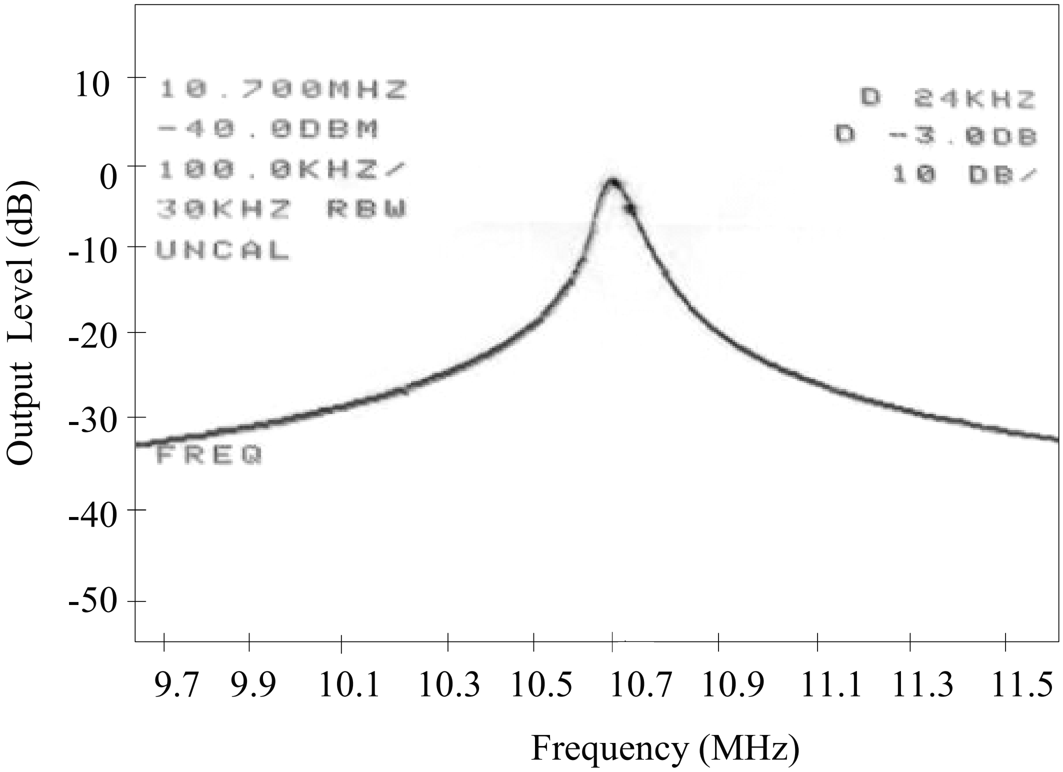

Figure 4.6 A measured frequency response at the center frequency f_0 =10.7 MHz and the quality factor Q_{HQ2} = 223 of Technique 2 shown in Figure 3.3.

4.4 Measured Current-Tunable Center Frequency f_o

4.4.1 Current-Tunable Center Frequency f_{o1} of Technique 1

Figure 4.7 shows plots of the center frequencies $f_{01} = \omega_{HQ}/(2\pi)$ and the corresponding quality factor Q_{HQ1} of Technique 1 shown in Figure 3.2 versus the bias current I_2 for three cases, i.e. the analysis, the PSPICE simulations, and the experimental results. It can be seen from Figure 4.7 that f_{01} is current tunable over 3 orders of magnitude. As expected, Q_{HQ1} essentially remains almost constant at approximately 121 and is, unlike existing approaches, independent of variables such as a center frequency. When $I_2 > 1$ mA, the center frrequency f_{01} drops with further increase of the bias current due to effects of parasitic capacitances at higher frequencies. Although the upper value of I_2 can be expected to be higher than 10 mA, the upper limit of the circuit prototypes has been set to 5 mA, for save operation of the current sources.

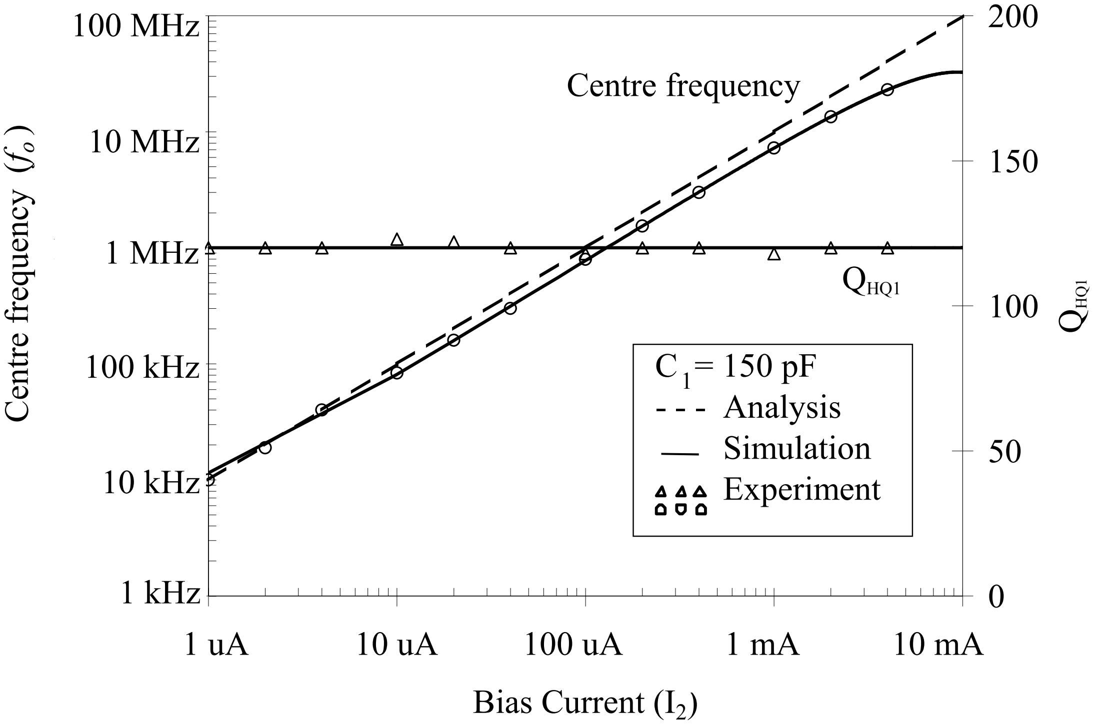

Figure 4.7 Plots of the center frequency f_0 and the quality factor Q_{HQ1} of Technique 1 shown in Figure 3.2 versus the bias current I_2.

4.4.2 Current-Tunable Center Frequency f_{o2} of Technique 2

Figure 4.8 shows plots of the center frequencies f_{02} and the corresponding quality factor Q_{HQ2} of Technique 2 shown in Figure 3.3 versus the bias current I_2 for three cases, i.e. the analysis, the PSPICE simulations and the experimental results. It can be seen from Figure 4.8 that f_{02} is also current tunable over 3 orders of magnitude in a similar manner to Technique 1 whilst Q_{HQ2} essentially remains almost constant at approximately 223 for $I_2 < 1$ mA. Again, when $I_2 > 1$ mA, the center frequency f_{02} drops with further increase of the bias current.

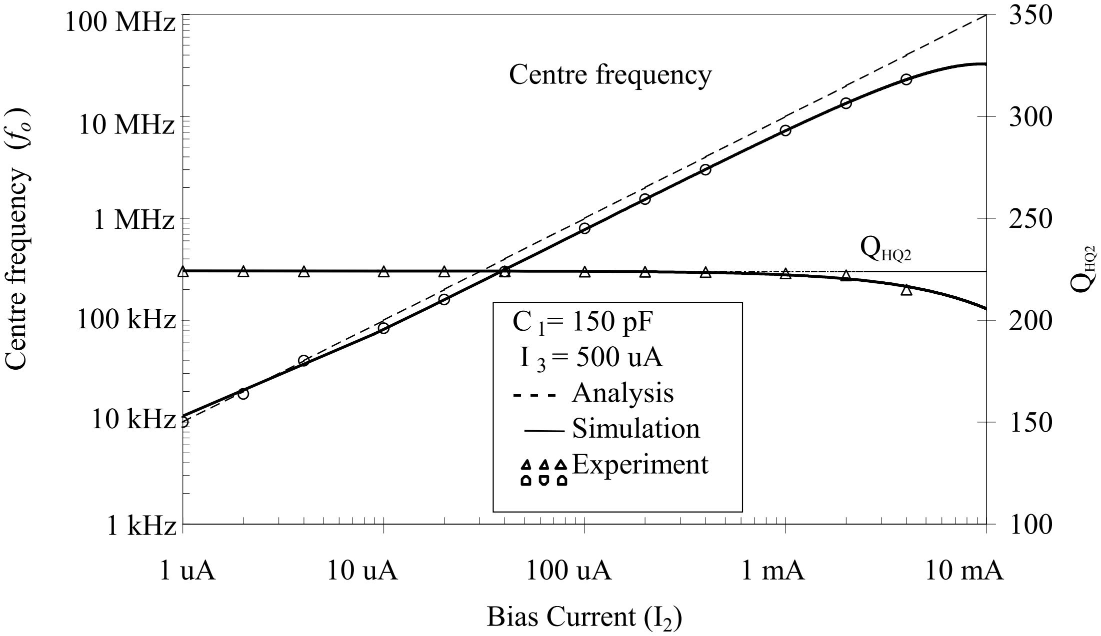

Figure 4.8 Plots of the center frequency $f_0 = \omega_{HQ}/(2\pi)$ and the quality factor Q_{HQ2} of Technique 2 shown in Figure 3.3 versus the bias current I_2.

4.5 Measured Noise Performance

Figure 4.9 shows the measured output noise spectrum shaped by the transfer function of Technique 1 shown in Figure 3.2, where the power noise density P_{N1} is relatively low at -

142.5 dBm/Hz and the resolution bandwidth (RBW) is at 100 kHz. Similarly, Figure 4.10 shows the measured output noise spectrum shaped by the transfer function of Technique 2 shown in Figure 3.3, where the power noise density P_{N1} is relatively low at –153.6 dBm/Hz and the resolution bandwidth (RBW) is at 300 kHz.

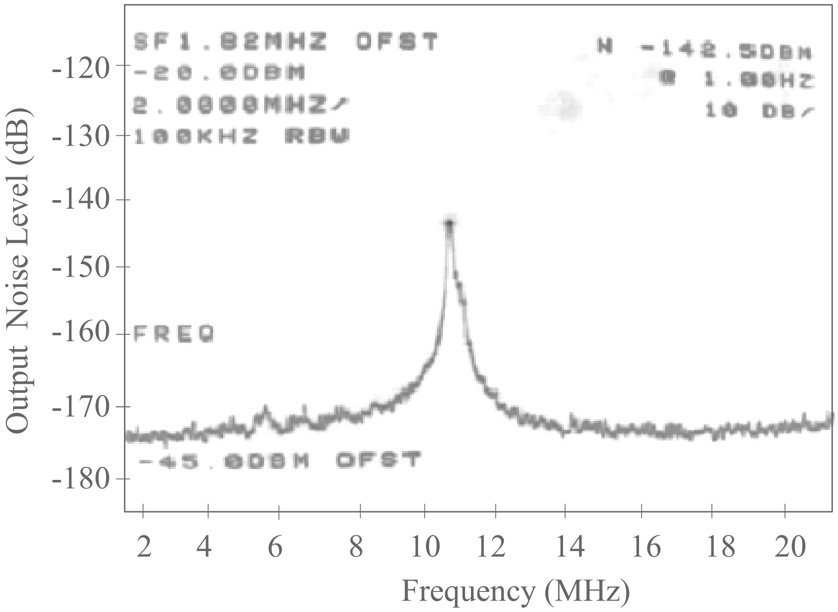

Figure 4.9 Measured output noise spectrum of Technique 1 shown in Figure 3.2.

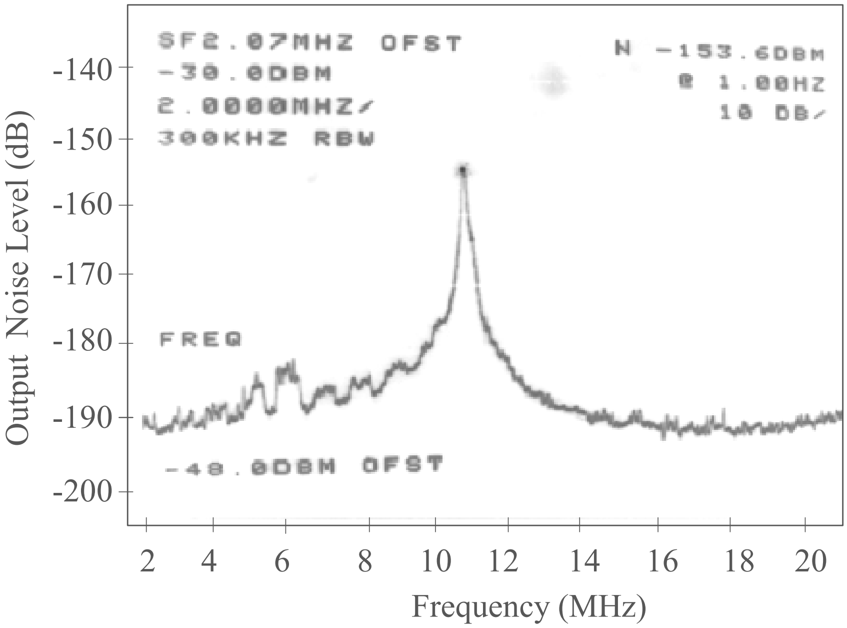

Figure 4.10 Measured output noise spectrum of Technique 2 shown in Figure 3.3

Table 4.1 Summaries of noise parameters obtained from Figures 4.9 and 4.10.

Parameters				Values		Units
				Technique 1 Figure 3.2	**Technique 2 Figure 3.3**	
(1)	Resolution bandwidth (RBW)			100	300	kHz
(2)	**Noise Density**	P_{N1}	10 log (P_{N2}/1mW)	–142.5	-153.6	dBm/Hz
		P_{N2}	-	5.6234×10^{-18}	4.3652×10^{-19}	W/Hz
		V_N^2	$P_{N2} \times (50\ \Omega)$	2.8117×10^{-16}	2.1826×10^{-17}	V^2/Hz
		V_{N1}	$\sqrt{(V_N^2)}$	1.6768×10^{-8}	4.6718×10^{-9}	$V_{rms}/\sqrt{Hz}$
(3)	**Total Noise**	V_{N2}	$V_N^2 \times RBW$	2.8117×10^{-11}	6.5477×10^{-12}	V^2
		V_{N3}	$\sqrt{V_{N2}}$	5.3026×10^{-6}	2.5589×10^{-6}	V_{rms}
		P_{N3}	$10 \log \frac{V_{N3}^2}{(50\Omega)(1\,mW)}$	–92.45	–98.82	dBm

Following Figures 4.9 and 4.10, Table 4.1 summarizes resulting noise parameters of both Techniques 1 and 2, in terms of (1) the resolution bandwidth, (2) the noise density and (3) the total noise. Some conclusions can be drawn from Table 4.1 as follows:

(a) For Technique 1 shown in Figure 3.2, the output noise density $V_{N1} = 0.016\ \mu V_{rms}/\sqrt{Hz}$, the total output noise $V_{N3} = 5.3026\ \mu V_{rms}$ and the total noise power P_{N3} = -92.45 dBm.

(b) For Technique 2 shown in Figure 3.3, the output noise density $V_{N1} = 0.004\ \mu V_{rms}/\sqrt{Hz}$, the total output noise $V_{N3} = 2.5589\ \mu V_{rms}$ and the total noise power P_{N3} = -98.82 dBm.

It can be observed from Table 4.1 that the total noise power of Technique 2 is lower than the total noise power of Technique 1. This can be expected because the use of the differential amplifier gain A_G and the positive feedback configurations in Technique 2 feeds back currents from the output to the input providing enhancement of the input current, thereby improving the overall noise (Liscidini et al., 2006).